Chapter-2

Experimental Techniques

2.1 Overview

This chapter deals with experimental methods and characterization techniques utilized in the thesis dissertation. This chapter explains sample preparation, fabrication methods, characterization techniques, and their working principles in detail.

This chapter consists of three sections:

(1) Different synthesis and materials fabrication techniques are involved in sample preparation.

(2) Characterization techniques used for crystal structure analysis, thermal analysis, and electrical analysis.

(3) Data analysis tools such as X-ray Rietveld refinement, microstructural study, Electrochemical study, impedance spectroscopy, and Machine Learning methods.

2.2 Materials Synthesis techniques

Different types of synthesis techniques have been presented in detail in this section. Mainly three different synthesis routes were followed in this thesis. The schematic representation of the three routes is explained in **Fig. 2.1**.

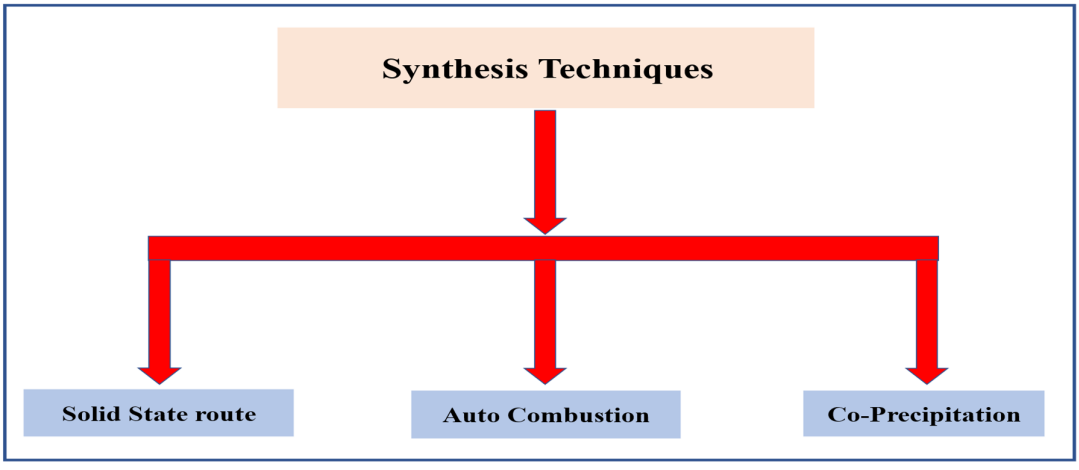

Figure 2.1*- Schematic representation of the three types of synthesis routes*

2.2.1 Solid-state or Ceramic method

The solid-state reaction serves as the method for synthesizing polycrystalline materials from solid reactants. This reaction takes place at elevated temperatures. Various factors influence the solid-state reaction, including the chemical and morphological characteristics of the reactants, such as their reactivity, surface area, and changes in free energy, as well as other conditions like temperature, pressure, and the surrounding environment. A significant benefit of this approach is its capacity for large-scale production. [1] A detailed block diagram in **Fig. 2.2** shows the steps involved in the synthesis.

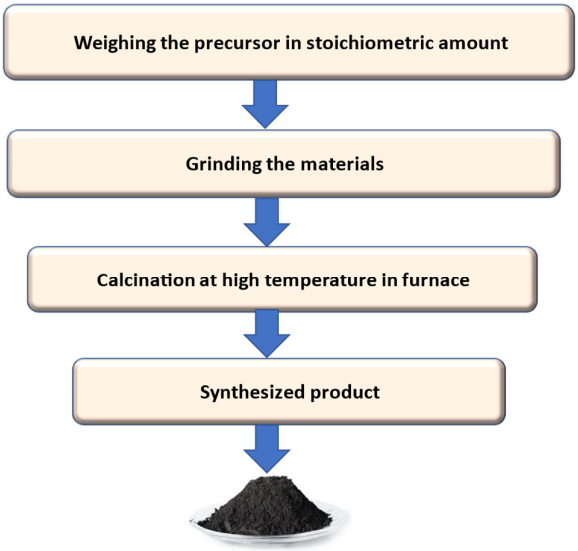

***Figure 2.2**- Block diagram of solid-state synthesis process or Ceramic method*

2.2.2 Sol-gel auto combustion method

Sol-gel auto-combustion is an efficient and economical synthesis method that facilitates the production of various metal oxides and nanoparticles. One of the key benefits of this technique is its ability to generate nano-sized materials that are homogeneous and exhibit a high degree of elemental mixing at the atomic scale. In this process, different types of fuels are employed for auto-combustion, allowing for the synthesis of desired products at

comparatively low temperatures [2]. Citric acid ($C_6H_8O_7$), Dextrose ($C_6H_{12}O_6$), sucrose ($C_{12}H_{22}O_{11}$), Urea (CH_4N_2O), Glycine ($C_2H_5NO_2$), etc are commonly used as fuels in the sol-gel auto combustion process. Urea, glycine, and citric acid form robust complexes with metal cations present in the solution. These fuels serve dual functions: (1) during combustion, they generate CO_2 and H_2O, which release heat in an exothermic reaction, and (2) they create complexes with metal ions, facilitating the homogeneous mixing of cations in the solution. Given that nitrogen does not engage in the redox reaction, it is believed to be released as a gas, thereby enhancing the porosity of the resulting materials. Additionally, the nature of the fuel significantly influences the intensity of the combustion reaction. [3] A detailed block diagram in **Fig. 2.3** shows the steps involved in the synthesis process.

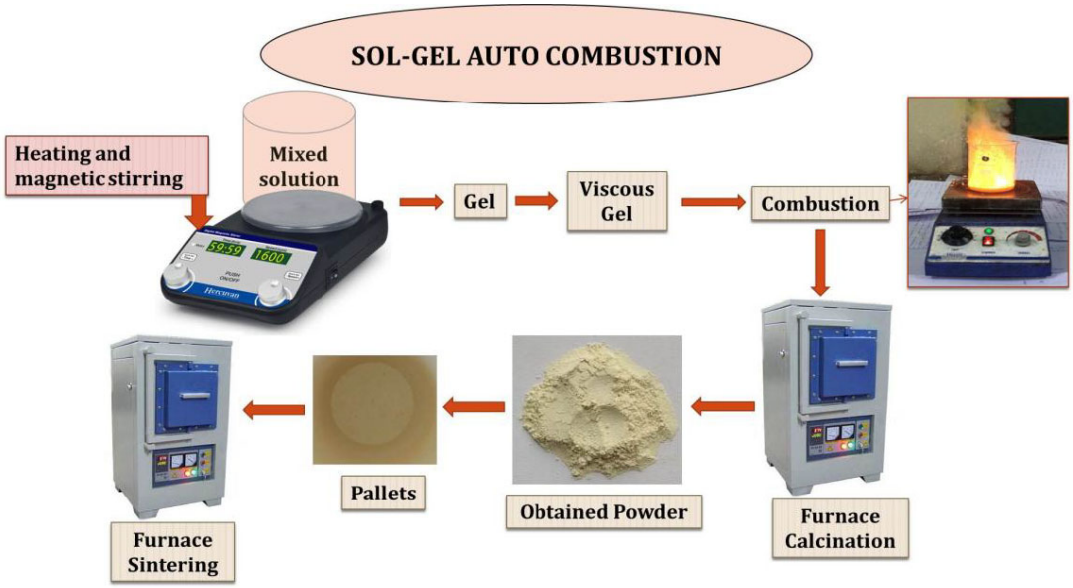

***Figure 2.3**- Block diagram sol-gel auto combustion synthesis process*

2.2.3 Co-precipitation method

The coprecipitation method entails the formation of metal precipitates as hydroxides or oxalates from a salt precursor, facilitated by the addition of a base in a solvent. The synthesis of monodispersed nanoparticles, achieved through the regulated release of anions

and cations, plays a crucial role in the kinetics of nucleation and particle growth. [4]. The management of chemical homogeneity and particle size presents challenges in the precipitation of mixed oxides. To address these issues, various modifications are employed, including the use of surfactants, sonochemical techniques, and high-gravity reactive precipitation, which assist in effectively regulating the morphological properties. Additionally, the precise control of experimental parameters—such as pH, reactant and ion concentrations, and temperature—plays a crucial role in the precipitation process. [5] A detailed block diagram in **Fig. 2.4** shows the steps involved in the synthesis.

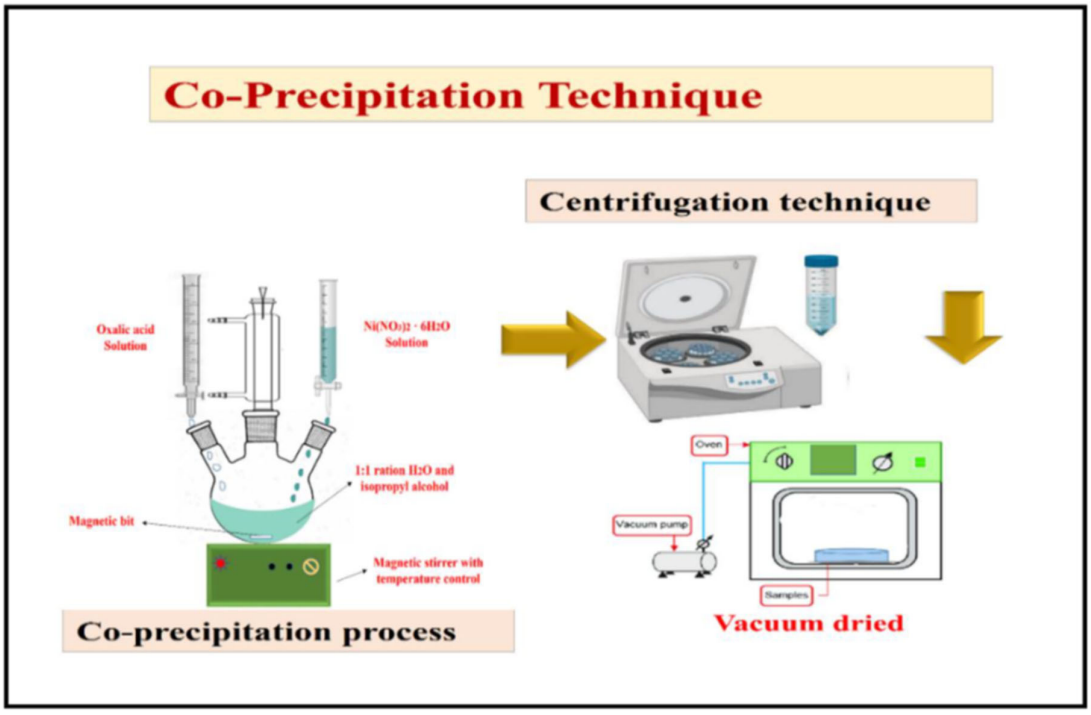

***Figure 2.4**-Block diagram Co-precipitation synthesis process*

2.3 Material Characterization Techniques

This section outlines the characterization techniques employed in this study. A brief overview of the fundamentals of each method will be provided in the subsequent section. The primary techniques are enumerated as follows.

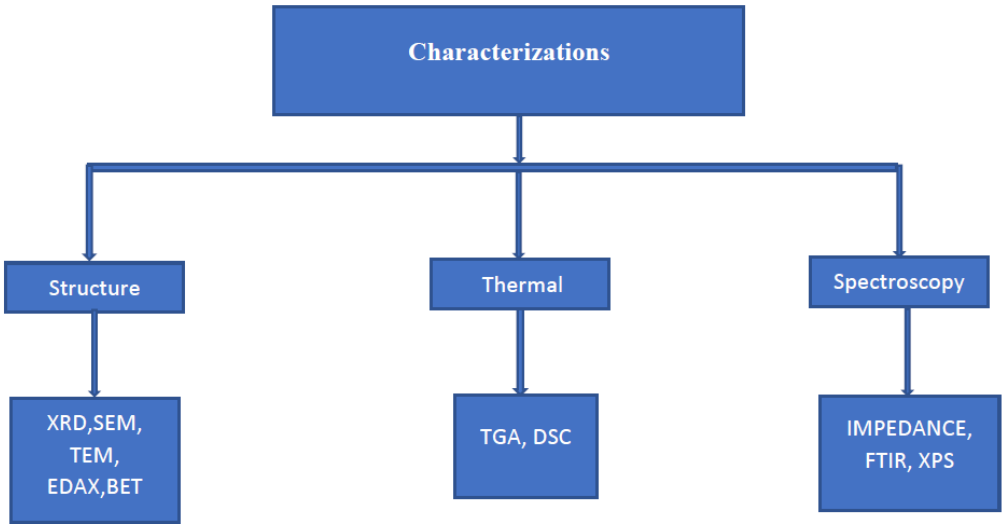

***Figure 2.5**- Characterization techniques used*

2.3.1 Powder X-Ray Diffraction (XRD)

X-ray diffraction (XRD) is a highly effective non-contact and non-destructive method, making it particularly suitable for structural investigations. This technique is capable of distinctly identifying the crystalline phases present within a material. It assesses various structural characteristics, including phase composition, grain size, preferred orientation, strain state, defect structure, and epitaxy of the phases found in the compound. The intensity data obtained from XRD can yield precise and quantitative insights into the atomic arrangements at interfaces. XRD is adept at identifying materials with varying elemental compositions; however, it exhibits heightened sensitivity to elements with high atomic numbers, as the diffracted intensities for these elements are significantly greater than those for elements with lower atomic numbers. This technique facilitates both quantitative phase analysis and qualitative assessments of structural and microstructural features.

The diffraction satisfies the Bragg equation:

$$n\lambda = 2dsin\theta \qquad (2.1)$$

Here d is the spacing between diffracting planes, is the incident angle, n is an integer, and λ is the beam's wavelength. [8-9]

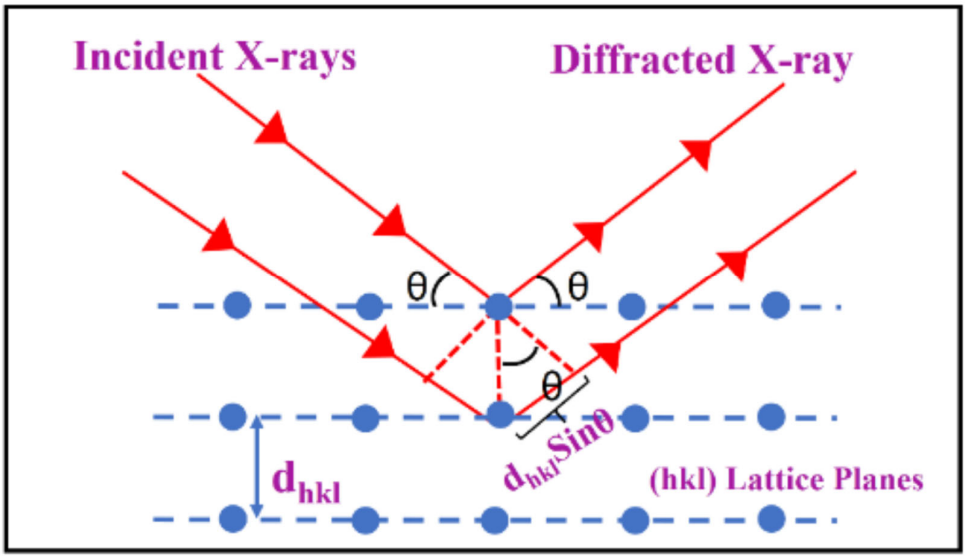

Figure 2.6*- Schematic diagram of the incident and diffracted X-rays from the crystal.[6]*

The XRD data were recorded in steps scan mode with a slow-scanning rate. The different phases were interpreted by recording an X-Ray diffraction pattern at room temperature on an X-Ray diffractometer (Rigaku Miniflex II, Japan) has Cu Kα radiation having wavelength λ= 1.5418 Å at an applied voltage of 40 kV and current of 40 mA. In this work, the XRD pattern has been recorded in the range of 10°-90° with a step size of 0.02°. The XRD setup is shown in **Fig. 2.7**.

2.3.2 Phase Confirmation and Crystal Structure Studies by Powder X-Ray diffraction

X-ray diffraction (XRD) is a highly adaptable, non-destructive method that provides comprehensive insights into the crystallographic structure of both natural and synthetic materials. The X-ray radiation predominantly utilized in this technique is emitted by copper, with the characteristic wavelength for Cu-Kα radiation being 1.5418 Å. When the incident beam interacts with a powder sample, diffraction takes place at all possible

orientations of 2θ. A movable detector, such as a Geiger counter linked to a chart recorder, can be employed to detect the diffracted beam.

Figure 2.7*- Rigaku, Miniflex II, Japan, XRD Set-up, IIT (BHU) Varanasi*

The configuration of the X-ray diffraction apparatus is illustrated in **Fig. 2.6**. Typically, the counter is programmed to scan a range of 2θ values at a consistent angular velocity. Generally, a 2θ range from 10 to 80 degrees is adequate to encompass the most significant portion of the powder pattern. The scanning speed of the counter is usually 2θ of 2° min^{-1}; therefore, about 30 minutes are needed to obtain a trace. Based on the principle of X-ray diffraction, a wealth of structural, physical, and chemical information about the material investigated can be obtained. A host of application techniques for various material classes are available, revealing the specific details of the sample studied.

Phase identification is the most essential application of X-ray diffraction studies, regardless of whether the unknown sample is single-phased or multi-phased. This identification aids

in comprehending the underlying mechanisms responsible for phase formation. Additionally, it provides insights into the relationship between crystal structure and various properties, commonly referred to as structure-property correlation, in accordance with Neumann's principle. [9]

Rietveld refinement is a widely used refinement technique for powder X-ray diffraction (XRD) based on the proposed method by Hugo Rietveld [10] in the 1960s. The Rietveld method involves fitting of a calculated profile (including all the structural and the instrumental parameters) to the experimental data. It employs the non-linear least-squares technique and requires a reasonable approximation of many free parameters in the initial stage, which includes peak shape, dimensions of the unit cell, and all the atomic coordinates in the structure of the crystal. Other parameters can be refined reasonably by guessing. The refinement of the crystal structure of a powdered material can be achieved through the analysis of PXRD data. The effectiveness of the refinement process is closely linked to the quality of the data, the quality of the model (which encompasses the initial approximation), and the expertise of the user.

A standard diffraction pattern is characterized by the locations, forms, and intensities of various Bragg reflections. Each of these three attributes conveys information pertinent to the crystal structure, the characteristics of the sample, and the features of the instrumentation used.

2.3.3 High-Resolution Scanning Electron Microscope (HR-SEM)

Electron microscopy represents a groundbreaking imaging technology that has been extensively utilized by both the scientific and engineering sectors to examine the morphology and structure of nanomaterials. The Nova NanoSEM 450 scanning electron microscope (SEM) was utilized to analyze the morphology of the prepared sample. In the SEM methodology, an electron beam is concentrated using various magnetic lenses and

apertures directed at the sample to generate an image. It is essential for the specimen to possess electronic conductivity in this measurement technique to prevent charging effects, which can lead to degraded image quality at elevated resolutions.

Pattern component	Crystal structure	Specimen property	Instrumental parameter
Peak position	Unit cell parameters (a, b, c, α, β, γ)	• Absorption • Porosity	• Radiation (wavelength), • Instrument/sample alignment • Axial divergence of the beam
Peak intensity	Atomic parameters (x, y, z, B, etc.)	• Preferred orientation • Absorption • Porosity	• Geometry and configuration • Radiation (Lorentz polarization)
Peak shape	• Crystallinity • Disorder • Defects	• Grain size • Strain • Stress	• Radiation (spectral purity) • Geometry • Beam Conditioning

***Table 2.1**: Powder diffraction pattern as a function of various crystal structure, specimen, and instrumental parameters [11]*

Fig. 2.8 shows the typical layout of HR-SEM, which consists of an electron gun from where the electrons are generated and accelerated via an accelerating anode, electromagnetic lenses for focusing the electrons, a vacuum chamber, and a detector to collect the signals emitted from materials [12]. The scattering occurs due to interaction between the high-energy electrons and the specimen, which results in the generation of different signals such as secondary electrons, backscattered electrons, characteristic X-rays, and auger electrons. The Auger electrons are generated from the surface of the sample in a low atomic number molecule.

The secondary electrons are generated by the inelastic scattering and they have energy around a few keV and backscattered electrons are generated by elastic scattering and have high energy. The imaging is done with the improved spatial resolution by the secondary

electron [12-13]. The image quality in SEM depends on the depth of field and the resolution, which can be affected by working distance, probe current, accelerating voltage, and astigmatism. The resolution in SEM is in the nanometer range**. Fig. 2.9** shows a picture of the HR-SEM facility at CIFC, IIT (BHU) Varanasi.

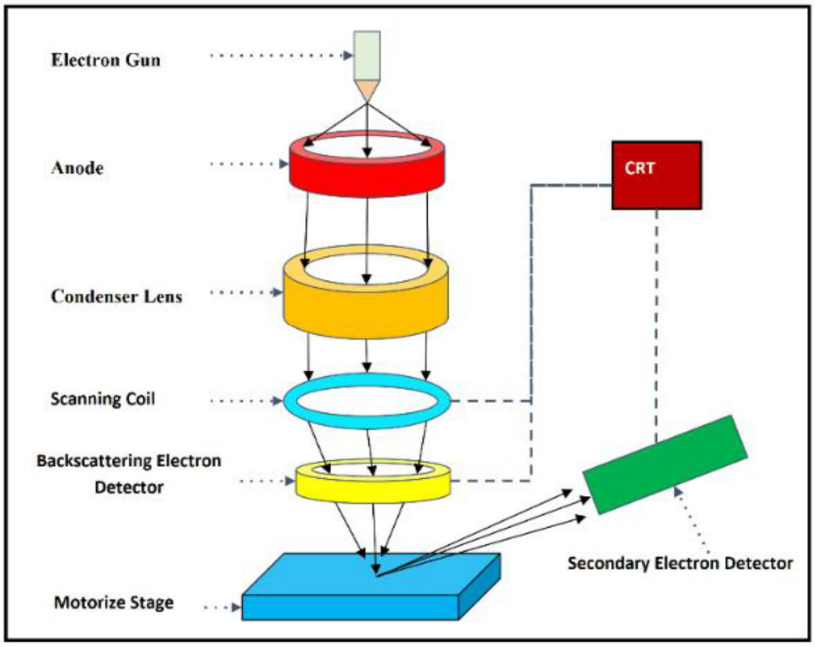

Figure 2.8- *Schematic diagram of the core component of SEM microscope [13].*

Figure 2.9*- HR-SEM Instrument facility, ZEISS EVO 18 in CIFC IIT (BHU) Varanasi*

2.3.4 High-Resolution Transmission Electron Microscope (HR-TEM)

The typical layout of HR-TEM is shown in **Fig. 2.10 (a)**, where the objective aperture is placed in the back focal plane of the objective lens. Transmitted and diffracted electrons are used by changing the aperture position for the bright-field and dark-field imaging modes in TEM as shown in **Fig. 2.10 (b)** and **Fig. 2.10 (c)**, respectively.

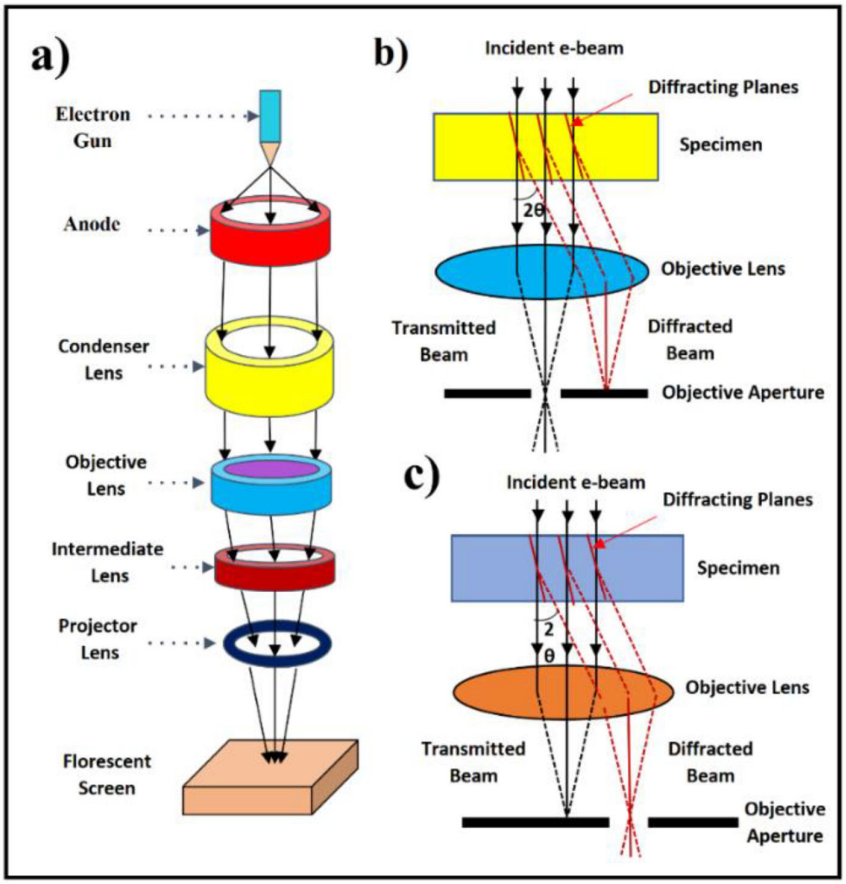

***Figure 2.10**- (a) Schematic diagram of core component of TEM microscope. Transmitted and diffracted electrons for (b) Bright field and (c) Dark field imaging in TEM [13] (Figure is taken from open access internet source)*

The electrons that are transmitted can traverse the aperture in bright-field mode, resulting in images that illustrate mass-thickness contrast. Conversely, in dark-field mode, the transmitted electrons are entirely obstructed by the aperture, allowing only the diffracted electron beam to pass through. This process yields insights into the crystal structure. [13,15]

In TEM, the specimen needs to be ultrathin (less than 100 nm) or a suspension of the material on a grid. The TEM has the highest resolution (atomic level) of any electron microscope and it has a magnification of 10 to 50 million times. **Fig. 2.11** shows the HR-TEM instrument installed in CIFC, IIT(BHU) Varanasi.

Figure 2.11- *HR-TEM Facilities with EDAX spectrometer, IIT (BHU) Varanasi*

2.3.5 Thermogravimetric analysis (TGA)

The thermogravimetric analysis (TGA) technique is primarily employed to assess the thermal stability of various oxide, nitride, and sulfide materials. This method involves recording the mass of a sample as a function of temperature, which allows for the observation of mass changes (either absorption or desorption), phase transitions, and thermal decomposition. When the mass of the sample remains unchanged within a specific temperature range, it is considered thermally stable in that range. Additionally, TGA aids in identifying the calcination temperature of the sample, indicating the maximum

temperature threshold at which degradation begins. [16] **Fig. 2.12** shows a picture of the TGA measurement system installed at IIT(BHU) Varanasi.

Figure 2.12*- TGA measurement system CIFC, IIT (BHU) Varanasi*

2.3.6 Fourier transform infrared (FTIR) spectroscopy

FTIR produces an infrared absorption spectrum to help of spectrum identify the presence of certain functional groups in a molecule. The spectrum of distinct molecular fingerprints can be used to screen and scan samples for many different components. FTIR detects functional groups and characterizes covalent bonding information. An FTIR spectrometer consists of a light source, monochromatic, slit, beam splitter, detector, and an analog recorder. The monochromator (e.g., a salt prism or grating with finely spaced lines) differentiates the source radiation into its different wavelengths. The slit selects the collection of wavelengths that pass through the sample at any given time. In a double-beam

operation, a beam splitter separates the incident beam in two; half goes to the sample and half to the reference. The sample absorbs light according to its chemical properties. The detector collects the radiation that passes through the sample and compares its energy to that going through the reference. The detector produces an electrical signal. A link between the monochromator and the detector allows the user to record energy as a function of frequency or wavelength. To improve the resolution, it is necessary to narrow the slit and decrease the sensitivity. Secondly, it is possible to run multiple scans to build up a signal-to-noise ratio. Finally, the instrument needs to be calibrated repetitively due to misalignment between the analog connection and the monochromator. [17-18]. **Fig. 2.13** shows the FTIR spectrometer installed at CIFC, IIT(BHU) Varanasi.

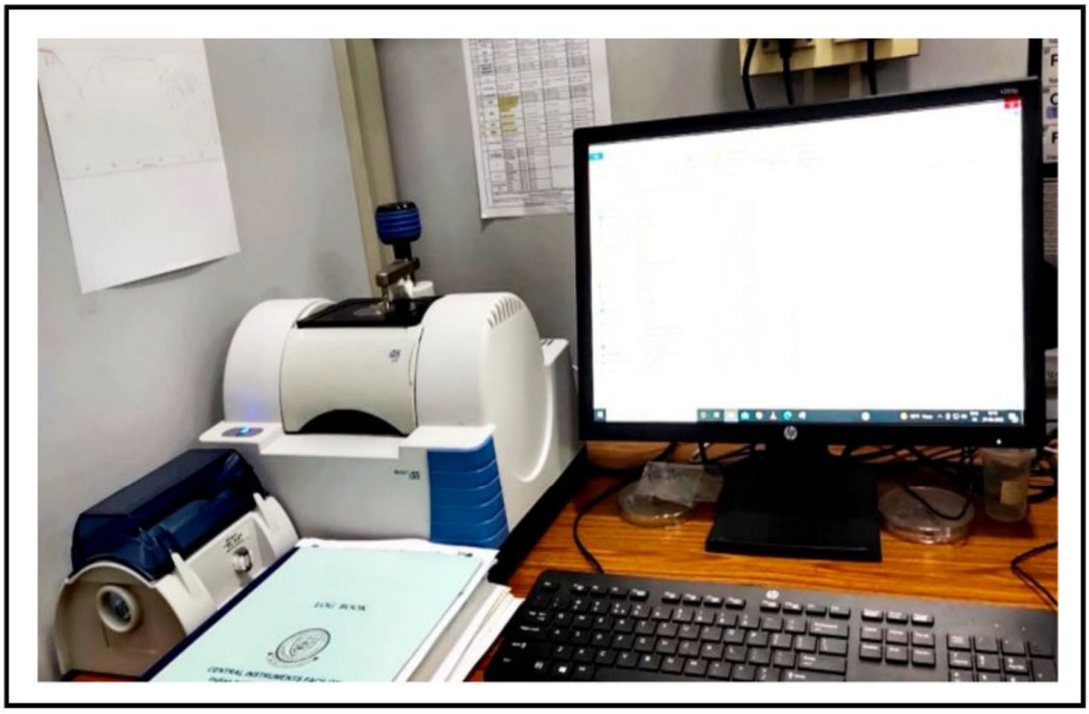

Figure 2.13- *FTIR spectrometer CIFC, IIT (BHU) Varanasi*

2.3.7 UV-Visible Spectrophotometer

This is a useful technique to determine the band gap and the absorption properties of materials within the visible and adjacent (near-ultraviolet and near-infrared) range. A

compound absorbs light in the UV-visible region and gets excited and the absorption spectra are used to determine the bandgap of the semiconductors. The absorbance is measured with respect to a reference and a graph of absorbance vs wavelength is plotted [19]. The schematic diagram of the UV-visible spectrophotometer is shown in **Fig. 2.14**. In this study difference between absorbed light intensities of sample and reference cell is measured to identify the absorption characteristic of the sample

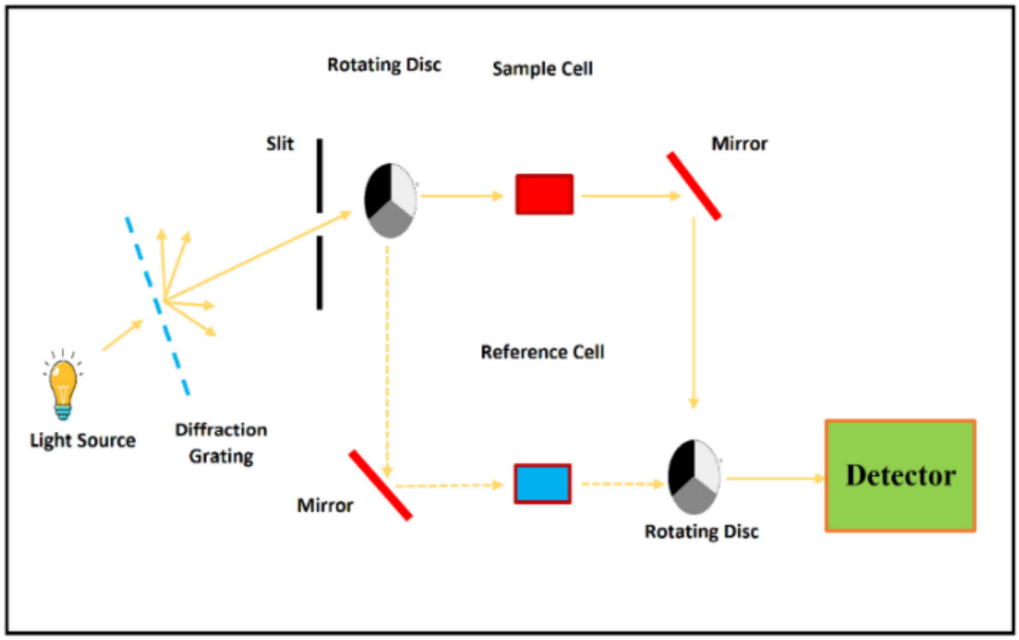

***Figure 2.14**- Schematic diagram of UV-Visible spectrometer [19]*

2.3.8 Raman Spectroscopy

Raman spectroscopy is a non-destructive powerful tool to characterize materials. Raman spectroscopy has been widely used to figure out the layer number and the defect in 2D materials. The basic principle of Raman spectroscopy is based on the interaction between electromagnetic field (EMF) and materials/molecules, which results in inelastic scattering. The incident EMF i.e. photons interact with the analytic molecule, and a dipole moment is induced which is directly proportional to the polarizability of the molecule. The shorter

wavelength laser possesses higher Raman scattering (inelastic scattering) cross-sections; hence it provides a greater signal. In Raman's study, inelastic scattering occurs when the incident photon wavelength is different from the scattered photon wavelength, the higher wavelength is stoked and the lower wavelength is the anti-stokes lines. The intensity of the Raman signal is very weak as compared to the incident laser, i.e., single inelastic scattering out of one million scatterings. A Raman spectrometer has mainly three components such as laser, the sampling interface, and the spectrometer as shown schematically in **Fig. 2.15** In the Raman system, fiber optics cables have been used to transmit and collect the signal from the specimen. To remove the Rayleigh signals, a notch filter is used and the remaining signals are passed through a dispersive holographic grating. To reduce the intensity of the incident monochromatic laser source, we have used a different neutral density filter. To detect the Raman signal, a high-quality CCD detector is used. [20-21]

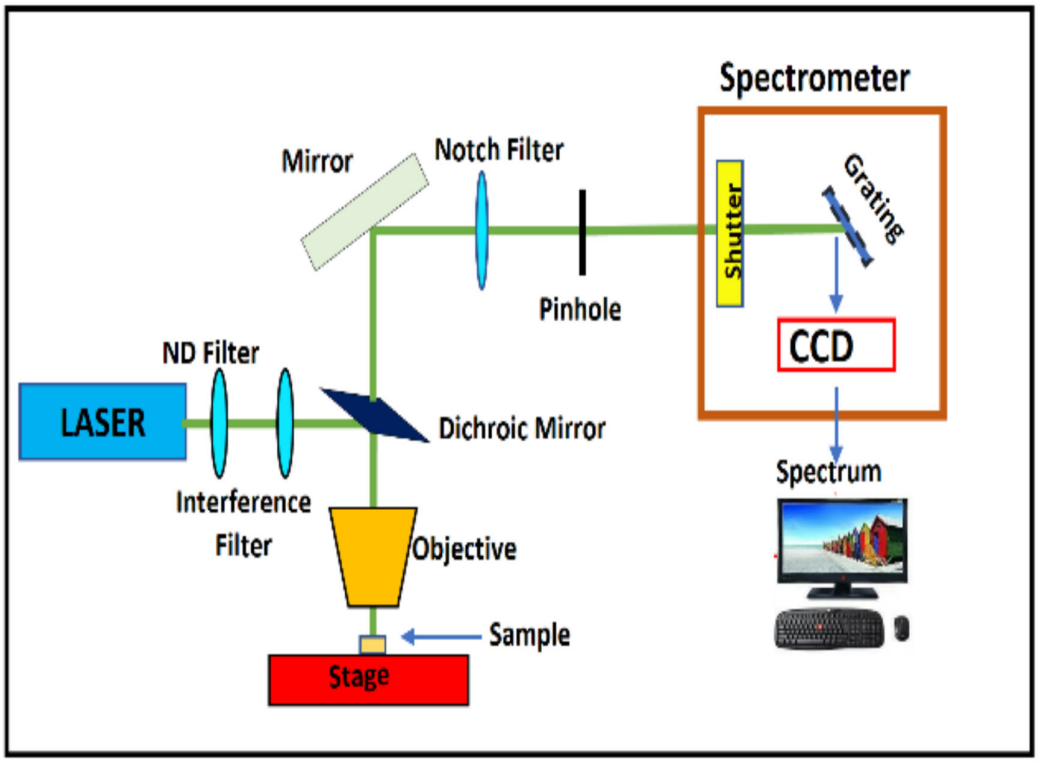

Figure 2.15- *Schematic diagram of Raman spectrometer*

2.3.9 X-ray photoelectron spectroscopy (XPS)

X-ray photoelectron spectroscopy (XPS) is a technique providing surface compositional information, electronic states, bond type, and valence of the elements. To perform XPS, the sample is bombarded with a beam of X-rays that has a narrow energy range. These X-rays are absorbed by the electrons associated with the atoms in the sample and some of the electrons are then ejected from the sample surface; the electrons are called photoelectrons. Photoelectrons are low energy and their escape depth is about 10 nm (near the surface region of a sample). The energy of the ejected electrons is measured and this gives information on the atomic species and the types of 46 bonds present in the sample. Based on the law of energy conservation, photoemission is described by the following equation: $E_k = h\nu - E_B$ where h is the Planck's constant, v is the frequency of the X-ray photon, Ek is the kinetic energy measured by the electron energy analyzer scanning the kinetic energy spectrum and EB represents the electron binding energy of the i-th level. By counting the number of electrons at different binding energies, an energy spectrum can be precisely produced via a pattern with intensity vs binding energy.

Figure 2.16- *X-ray photoelectron spectroscopy (XPS), CIFC. IIT(BHU)*

The specific binding energy of the electron acts as the blueprint to identify the composition of the sample with the intensity corresponding to the quantity of the element. High resolution (HR)-XPS can be achieved using an additional monochromator in the XPS system to reduce energy width dispersion. Additionally, lower spectral background and the elimination of unwanted X-rays can also be accomplished. The detection limit for the XPS is usually in the parts per thousand range. However, higher resolution can be obtained with extended signal collection time [22].

2.3.10 BET (Brunner-Emmett-Teller theory) surface area measurement

BET determines the specific surface area and pore size distribution of the material. Those surface areas will further assist to understand the catalytic activity, moisture retention, and shelf life. BET utilizes the physical adsorption of gas (nitrogen gas) on the surface of a solid to determine its specific surface area. Physical adsorption involves van der Waals force between adsorbate and adsorbent. After adsorption of gases desorption will occur. Hence the amount of adsorption of a gas on the adsorbent will determine the required specific surface area of the sample. BET process is usually carried out at constant temperature or under the isothermal condition which was maintained by liquid nitrogen.

Figure 2.17- *BET (Brunner-Emmett-Teller theory), CIFC. IIT(BHU)*

On the other side, the pressure or the concentration of the adsorbate gas kept on increasing. Therefore, graph has been plotted between the relative pressure of the gas and volume adsorbed onto the sample. [23-24]

BET is carried out in three-step:

1. Standardisation of the reference cell.

2. Pre-treatment of the sample by heating at a specific temperature.

3. Adsorption of adsorbate onto the adsorbent under isotherm conditions.

2.4 Electrochemical Measurements

Electrochemical measurements are employed to assess the electrochemical performance of the electrode developed for the supercapacitor. Three primary techniques utilized for evaluating this performance include cyclic voltammetry (CV), galvanostatic charge-discharge (GCD), and electrochemical impedance spectroscopy (EIS).

2.4.1 Electrode fabrication

The active materials (different types of oxide materials utilized in the study), carbon black and polyvinylidene fluoride (PVDF) powders are pre-weighed before mixing them.

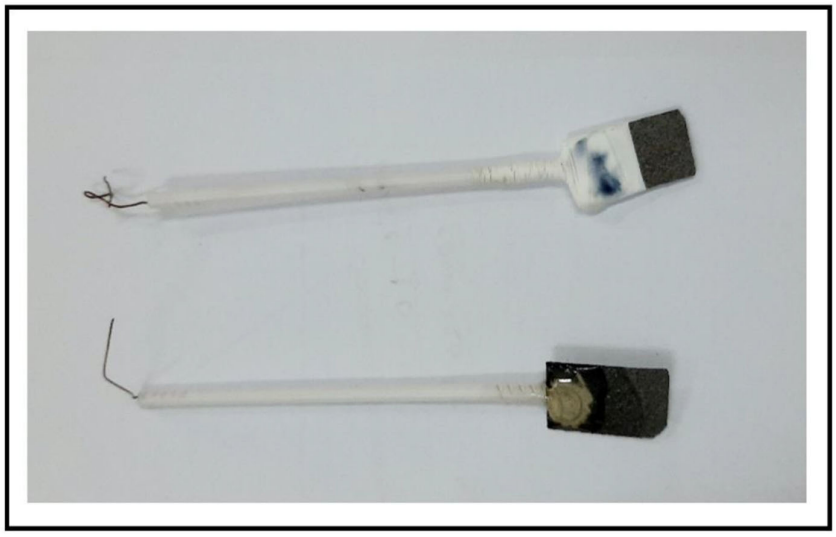

Figure 2.18- *Electrode picture for supercapacitor application*

The three ingredients are ground thoroughly in a mortar followed by the addition of a small amount of N-methyl pyrrolidinone (NMP) solution to form a slurry. For supercapacitor application, the slurry is then applied (area of coating: 1 cm^2, and a total mass of around 1 mg) uniformly onto Carbon Toray paper with help of a micropipette. The fabricated electrodes are immediately transferred to an electric oven and dried at 90o C under vacuum overnight. **Fig. 2.18** shows the prepared electrode for the study.

2.4.2 Cyclic Voltammetry (CV)

Cyclic voltammetry (CV) is the predominant characterization method employed in analytical chemistry for examining the thermodynamics of redox reactions, the kinetics of electron transfer reactions, and the behaviour of substrate adsorption on electrodes. In the realm of electrochemistry, it serves to analyse redox reaction dynamics and to assess the specific capacitance and stability of electrode materials. Voltammograms represent the relationship between the potential window and current density, generated by recording the current at the working electrode during a continuous potential scan.

The three-electrode system serves as the fundamental configuration for examining the electrochemical properties of a sample. This system comprises a working electrode (WE), a counter electrode (CE), and a reference electrode (RE). The potentiostat regulates the potential difference between the WE and CE while simultaneously measuring the potential difference between the WE and RE. Functioning as a galvanostat, the device manages the current flow between the WE and CE. The software known as NOVA1.1 continuously analyses the potential difference of the WE in relation to the RE and the current flowing between the CE and WE. Consequently, the graph generated that depicts the relationship between specific current and potential difference is referred to as a "Cyclic Voltammetry" plot. [25]

The working electrode is an electrode over which the reaction of interest is occurring. Mostly glassy carbon, graphite sheet, and carbon paper can be used as a current collector over which active material/working electrode has been coated. The counter electrode exhibits inert behavior such as Platinum, gold, graphite, and glassy carbon which generally doesn't involve in the electrochemical reaction. The current circuit of the electrochemical cell has been closed using these counter electrodes. Reference electrodes are those electrodes whose electrode potentials are well known such as Ag/AgCl and saturated calomel electrode (SCE).

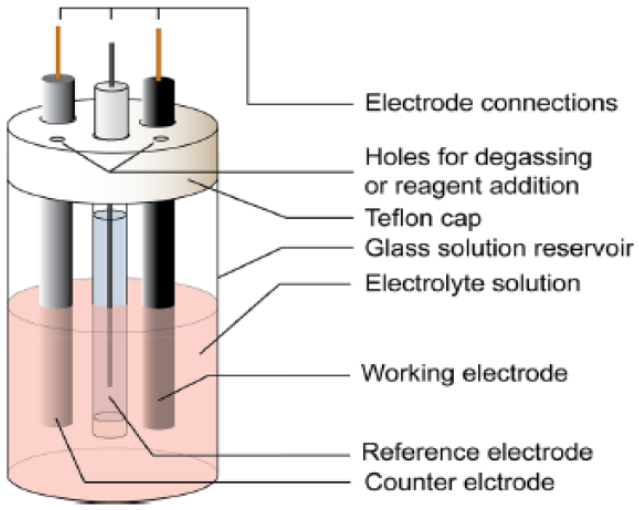

Figure 2.19*- Conventional three electrodes setup used in electrochemical testing*

2.4.3 Galvanostatic Charge-Discharge (GCD)

Similarly, the cyclic voltammetry technique, GCD technique is used for measurement of electrochemical performance of supercapacitor electrode through charge and discharge cycle in a controlled current condition. In the GCD technique, the current is regulated while the voltage is recorded at the working electrode, with the resulting voltage being referenced against a reference electrode over time. Upon the application of current, the potential experiences a sudden change due to internal resistance, followed by a gradual alteration as over-potential builds up at the electrode, resulting from the depletion of reactant

concentration at the electrode surface. The GCD method allows for the calculation of parameters such as specific capacitance, resistance, and cyclability. The voltage equation pertinent to GCD is provided below:

$$(t) = iR + \frac{t}{c} i(V) \qquad (2.2)$$

From the charge-discharge curve, the specific capacitance of the electrode can be calculated as: [25]

$$C_{sp} = \frac{I\Delta t}{m\Delta V} \qquad (2.3)$$

2.4.4 Electrochemical Impedance Spectroscopy (EIS)

Electrochemical Impedance Spectroscopy (EIS) was performed to investigate the cyclic capacity or capacitance degradation associated with pseudocapacitance. The results from the EIS measurement were represented in a graph, with imaginary impedance ($Z_{imaginary}$) plotted on the y-axis and real impedance (Z_{real}) on the x-axis, commonly referred to as a "Nyquist plot." Typically, EIS measurements reveal a semi-circular pattern that spans from the high-frequency range to the low-frequency range.

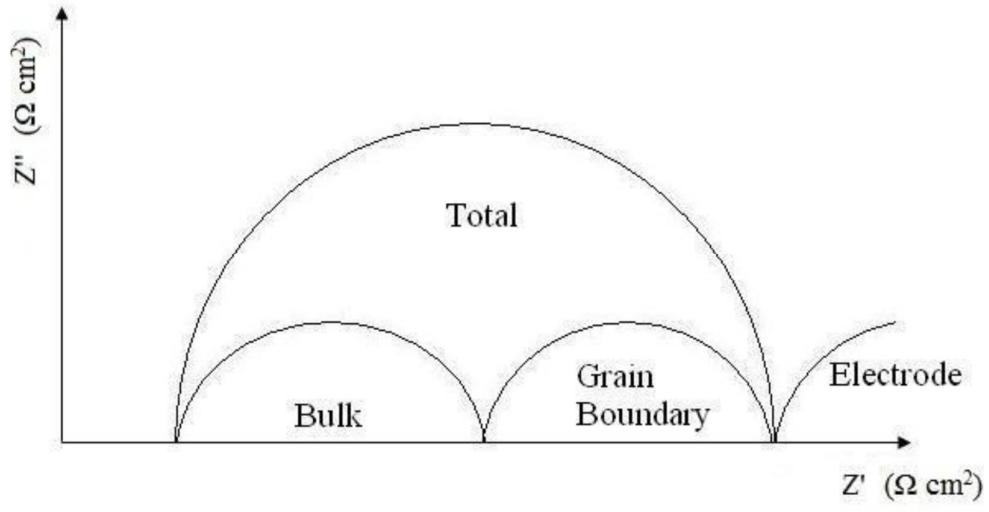

Figure 2.20- *Nyquist Plot for ionic solids (Z‘‘ = imaginary impedance, Z‘ = real impedance) [26].*

In this work, the electrochemical stability test performed AC EIS measurements shown in the Nyquist plot at OCP in the frequency range (1 MHz to 0.1 Hz). The specific impedance contribution is mainly attributed to the impedance distributions over electric series resistance (R_s), charge transfer resistance (R_{ct}), and Warburg impedance (R_w). At higher frequency, the intercept in the EIS spectra on the real axis indicates very small internal resistance. The small semicircle in the high-frequency region also shows the fast charge transport between electrode and electrolyte. Lower frequency data represent the Warburg diffusion resistance, the straight line in the low-frequency region is close to 90º angle (very close to -Z"(Ω) axis) from the horizontal line represents the characteristic of pseudo capacitance behaviour. This also represents fast ion diffusion in the porous structure [22].

2.4.5 Chemical Kinetic for pseudocapacitors from Cyclic voltammetry (CV) curve

The classification of supercapacitors can be determined through their Current-Voltage response. This section examines the kinetics of pseudocapacitance as revealed by the cyclic voltammetry polarization curve,

1. Linear or pseudo linear relationship between the applied potential and state of charge (capacitance, dQ/dV)
2. Nearly ideal electrochemical reversibility
3. Surface-controlled kinetics

Lindström et al. Studied kinetics of Li^+ insertion into nano, porous anatase TiO_2 films and they found a relationship between the applied sweep rate and observed electrochemical current, they introduced b-value analysis. b value determines the presence of surface controlled/ capacitive (vs. semi-infinite diffusion-controlled) kinetics:[27]

$$i(V) = a\nu^b \qquad (2.4)$$

Where $i(V)$ is the current at a specific potential, sweep rates ν. a and b are adjustable parameters, and the b value can be determined as the slope of log(i) vs log(ν) for various

sweep rates. When b = 1 is denoted surface control and 0.5 denoted diffusion control. When the b-value falls between 0.5 and 1, the mechanism is attributed to a combination of diffusion and capacitive contributions b-value presentation shown in **Fig. 2.21.**

Liu et al. proposed a linear combination of surface- and diffusion-controlled currents [24]

$$i(V) = k_1(V)\,v + k_2(V)\,v^{1/2} \qquad (2.5)$$

Dunn et al. utilized this concept to deconvolute capacitive vs diffusive contributions to the total current for many types of nanostructured transition metal oxides. [28-30]

$$i(V)/v^{1/2} = k_1(V)\,v^{1/2} + k_2(V) \qquad (2.6)$$

k_1 and k_2 determine surface and diffusion-controlled processes at specific potentials with multiple sweep rates. The method allows for the separation of the cyclic voltammograms into surface-controlled and diffusion-controlled regions.

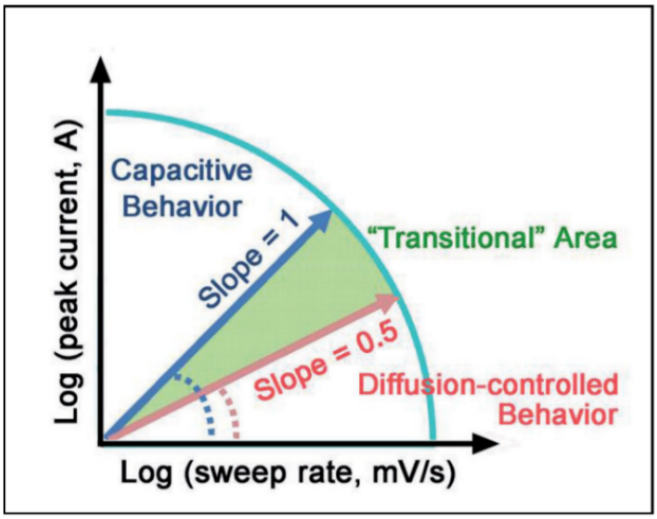

Figure 2.21- *Power-law dependence of the peak current on sweep rate for capacitive materials (b= 1.0) and typical battery-type materials (b = 0.5). The "transition" area between capacitive and battery-type materials area is located in the range of b = 0.5–1.0. [27] (Figure is taken from open access internet source)*

Trasatti et al. developed another new method based on voltammetric charge to deconvolute the "inner" (less accessible) and "outer" (more accessible) surface contributions. [31]

According to Trasatti, voltammetric charge (Q) can be divided into surface-controlled and diffusion-controlled contributions,

$$Q = Qs + Qd \qquad (2.7)$$

Where Qs and Qd are the surface-controlled and diffusion-controlled contributions to charge, respectively. Surface-controlled charge contribution also be divided into the "inner" surface contribution, Qs, in, and "outer" surface contribution,

$$Qs = Qs, in + Qs, out \qquad (2.8)$$

The "inner" surface contribution is sweep rate dependent (due to lower accessibility of redox sites) and the outer" surface contribution is invariant of sweep rate, Assuming semi-infinite linear diffusion and a linear relationship between Q_d and $\nu^{-1/2}$, equation (2.8) can be rearranged to determine Q_s, out when

$$Q = Q_{s,\,out} A1 + \nu^{-\frac{1}{2}} \qquad (2.9)$$

Where A1 is a constant. The y-intercept ($\nu^{-1/2} = 0$; or $\nu = \infty$) determines Qs. On the other hand, Qs is determined when $\nu = 0$. Assuming Q^{-1} decreases linearly with $\nu^{1/2}$, equation 2.9 is rewritten as

$$Q^{-1} = Q_s^{-1} A_2 \nu^{1/2} \qquad (2.10)$$

Where A_2 is another constant. Qs^{-1} can be obtained from the y-intercept ($\nu 1/2 = 0$)

2.5 Machine Learning (ML) driven study

In the field of machine learning, systems utilize past experimental data and established knowledge to develop models for predictive purposes. Recently, machine learning techniques have garnered significant attention due to their efficacy in predicting physical and chemical properties [32-33], conducting high-throughput screening for crystal structure predictions [34-35], uncovering relationships between structure and properties [36], and accelerating the synthesis of high-performance materials [37-38]. There has been an increasing focus on employing machine learning models to accurately forecast material

properties. The insights generated by these models not only illuminate the characteristics of the materials under examination but also offer guidance for future experimental endeavours.

2.5.1 Workflow of machine learning

The prediction or classification of materials utilizing a machine learning model is primarily influenced by the dataset collection, the choice of specific features, and the algorithms employed in the model. A standard workflow for constructing a machine learning model is illustrated in **Fig. 2.22**. The subsequent sections provide a detailed explanation of the steps involved.

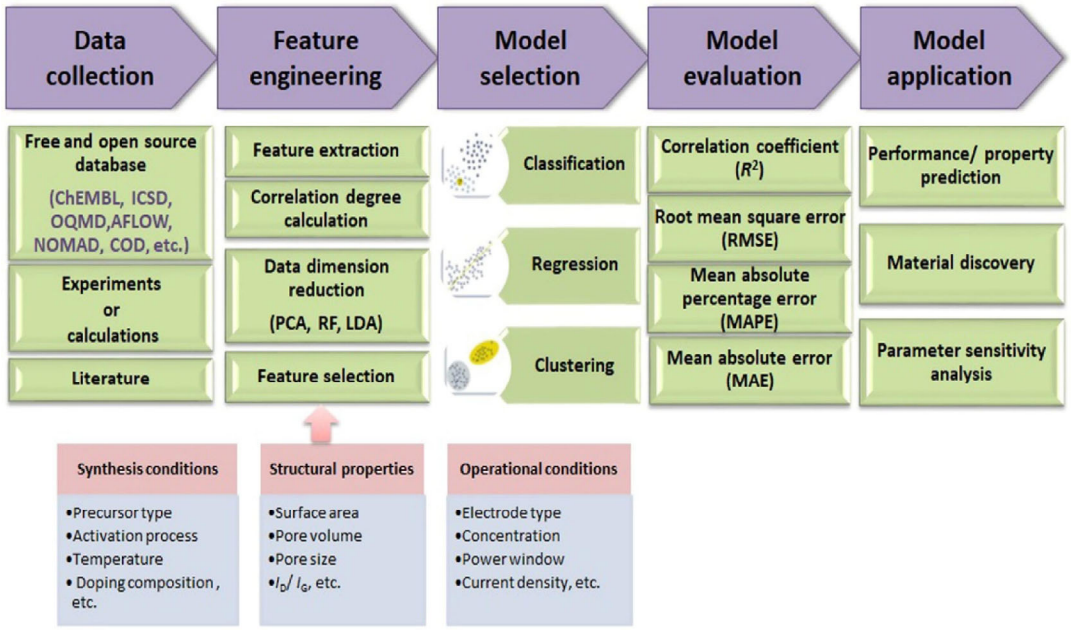

Figure 2.22- *Workflow of ML application [39] (Figure is taken from open access internet source)*

2.5.1.1 Data collection

Extensive datasets required for experimentation are sourced from open-access databases such as ChEMBL, ICSD, OQMD, and COD, as well as initiatives like the Materials Genome Initiative. These databases provide information on the electrical, optical, and

mechanical properties of materials. In order to predict the performance of supercapacitors, datasets are typically gathered from experimental studies, scientific literature, or computational analyses.

2.5.1.2 Feature engineering

Feature engineering involves the identification and selection of specific attributes or characteristics of materials, as well as the transformation of raw data into relevant features or quantitative metrics that effectively predict or classify information. This process encompasses feature extraction, calculation of correlation degrees, reduction of data dimensions, and selection of features. In the context of predicting the performance of supercapacitors, various synthesis conditions (such as precursor type, activation temperature, and activation method), structural characteristics of supercapacitor materials (including composition, morphology, specific surface area (SSA), pore volume (PV), pore size (PS), ID/IG ratio, and doping elements), along with operational parameters (like power window (PW), current density, and electrolyte type and concentration) serve as input features for training machine learning models.

2.5.1.3 ML model selection

Machine learning methodologies are classified into four main categories: supervised learning, unsupervised learning, reinforcement learning, and ensemble learning. The identification of the most suitable machine learning model, paired with an appropriate training dataset, is crucial for achieving high levels of prediction accuracy. In the field of material science, various supervised learning models, including artificial neural networks (ANN), support vector machines (SVM), decision trees (DT), multi-layer perceptrons (MLP), random forests (RF), linear regression (LR), recurrent neural networks (RNN), and Gaussian process regression (GPR), are frequently employed. Numerous previous studies

have successfully utilized ANN and RNN models to predict the performance of supercapacitors.

2.5.1.4 ML model evaluation

Machine learning models undergo evaluation and validation of their predictive outcomes using various performance metrics, including R, the correlation coefficient (R^2), root mean square error (RMSE), mean absolute error (MAE), mean square error (MSE), mean absolute percentage error (MAPE), and error rate. In addition to these parameters, each machine learning model is characterized by hyperparameters that influence its overall performance.

References

1. Youssef Ben Smida, Riadh Marzouki, Savaş Kaya, Sultan Erkan, Mohamed Faouzi Zid and Ahmed Hichem Hamzaoui, Synthesis Methods in Solid-State Chemistry, 7th, 2020, 10.5772/intechopen.93337
2. Kessler, V. G., Seisenbaeva, G. A., Unell, M. & Hakansson, S. Chemically Triggered Biodelivery Using Metal-Organic Sol-Gel Synthesis. Angew. Chem. Int. Ed. 47, 8506–8509 (2008)
3. Dumitrescu, P. Samoila, V. Nica, F. Doroftei, A. Iordan, M. Palamaru Study of the chelating/fuel agents influence on NiFe2O4 samples with potential catalytic properties Powder Technol., 2013, 243, 9-17
4. U.P.M.Ashik, Shinji Kudo Jun-ichiroHayash, Synthesis of Inorganic Nanomaterials , Advances and Key Technologies Micro and Nano Technologies 2018, 19-57
5. Hans-Christian Rotha, S. P.Schwamingera, Michael Schindlera Friedrich E.Wagnerb Sonja Berensmeier, Influencing factors in the CO-precipitation process of superparamagnetic iron oxide nanoparticles: A model-based study, Journal of Magnetism and Magnetic Materials, 2015, 377, 81-89
6. G. Jeffery, "Elements of X-Ray Diffraction (Cullity, BD)," Journal of Chemical Education, vol. 34, pp. A178, 1957
7. Borie, B. X-Ray Diffraction in Crystals, Imperfect Crystals, and Amorphous Bodies. Journal of the American Chemical Society. 1965, pp 140–141.
8. B. D Cullity, Elements of X- Ray Diffraction.
9. Bunaciu, A.A., UdriŞTioiu, E.G. and Aboul-Enein, H.Y., 2015. X-ray diffraction: instrumentation and applications. Critical reviews in analytical chemistry, 45(4), pp.289-299.
10. Rietveld, H. M. (2 June 1969). "A profile refinement method for nuclear and magnetic structures". Journal of Applied Crystallography. 2 (2): 65–71.
11. Pecharsky, V. K., & Zavalij, P. Y. (2009). Fundamentals of Powder Diffraction and Structural Characterization of Materials
12. L. Chen, J. Xu, and J. Chen, "Applications of Scanning Electron Microscopy in Earth Sciences," Science China-Earth Sciences, vol. 58, pp. 1768-1778, 2015.
13. B.J. Inkson, "Scanning Electron Microscopy (SEM) and Transmission Electron Microscopy (TEM) for Materials Characterization," Materials Characterization Using Nondestructive Evaluation (NDE) Methods, Elsevier, pp. 17-43, 2016.

14. W. Wan, J. Su, X. D. Zou, and T. Willhammar, "Transmission Electron Microscopy as an Important Tool for Characterization of Zeolite Structures," Inorganic Chemistry Frontiers, 2018, 5, 2836-2855

15. V. E. Cosslett, "Transmission Electron-Microscopy - Physics of Image-Formation and Microanalysis - Reimer, L," Nature, vol. 309, pp. 186-186, 1984

16. Francis C. Mayville, Rodney J. Wigent & Joseph B. Schwartz, Thermogravimetric Analysis for the Determination of Water Release Rate from Microcrystalline Cellulose Dry Powder and Wet Bead Systems, Pharmaceutical Development and Technology, 2006, 11:359–370

17. J. Griffiths and J. A. De Haseth, Fourier Transform Infrared Spectrometry, John Wiley & Sons, 2007

18. Suart, B. Infrared spectroscopy: Fundamental and applications. Wiley: Canada, 2004; 15:1-242.

19. F. S. Rojas and C. B. Ojeda, "Recent Development in Derivative Ultraviolet/Visible Absorption Spectrophotometry: 2004-2008," Analytica Chimica Acta, vol. 635, pp. 22-44, 2009.

20. P. K. Kannan, P. Shankar, C. Blackman, and C. H. Chung, "Recent Advances in 2D Inorganic Nanomaterials for SERS Sensing," Advanced Materials, vol. 31, pp. 1803432-183458, 2019

21. A. Balcytis, Y. Nishijima, S. Krishnamoorthy, A. Kuchmizhak, P.R. Stoddart, R. Petruskevicius, and S. Juodkazis,"From Fundamental toward Applied SERS: Shared Principles and Divergent Approaches," Advanced Optical Materials, vol. 6, pp.1800292-1800320, 2018.

22. P. Van der Heide, X-ray photoelectron spectroscopy: an introduction to principles and practices. John Wiley & Sons

23. Sing, K. S. Adsorption methods for the characterization of porous materials. Advances in Colloid and Interface Science, 1998, 76, 3-11.

24. Donohue, M. D.; Aranovich, G. L., Classification of Gibbs Adsorption Isotherms. Adv. Colloid Interface Sci. 1998, 76, 137-152.

25. N. Elgrishi, K.J. Rountree, B.D. McCarthy, E.S. Rountree, T.T. Eisenhart, J.L. Dempsey, A Practical Beginner's Guide to Cyclic Voltammetry, J. Chem. Educ. 95 (2018) 197–206.

26. A. Bitar, C. Kaewsaneha, M.M. Eissa, T. Jamshaid, P. Tangboriboonrat, D. Polpanich, A. Elaissari, Ferrofluids: from preparation to biomedical applications, J. Colloid Sci. Biotechnol. 3 (2014) 3–18.

27. Liu, T.-C.; Pell, W. G.; Conway, B. E.; Roberson, S. L. Behavior of Molybdenum Nitrides as Materials for Electrochemical Capacitors Comparison with Ruthenium Oxide. J. Electrochem. Soc. 1998, 145, 1882−1888

28. Brezesinski, T.; Wang, J.; Senter, R.; Brezesinski, K.; Dunn, B.; To lbert, S. H. On the Correlation between Mechanical Flexibility, Nanoscale Structure, and Charge Storage in Periodic Mesoporous CeO2 Thin Films. ACS Nano 2010, 4, 967−977.

29. Brezesinski, K.; Wang, J.; Haetge, J.; Reitz, C.; Steinmueller, S. O.; Tolbert, S. H.; Smarsly, B. M.; Dunn, B.; Brezesinski, T. Pseudocapacitive Contributions to Charge Storage in Highly Ordered Mesoporous Group v Transition Metal Oxides with Iso-Oriented Layered Nanocrystalline Domains. J. Am. Chem. Soc. 2010, 132, 6982− 6990.

30. Ardizzone, S.; Fregonara, G.; Trasatti, S. Inner‖ and ―Outer‖ Active Surface of RuO2 Electrodes. Electrochim. Acta 1990, 35, 263−267

31. Zheng, J. P.; Cygan, P. J.; Jow, T. R. Hydrous Ruthenium Oxide as an Electrode Material for Electrochemical Capacitors. J. Electrochem. Soc. 1995, 142, 2699−2703

32. Kumar, N., Kumar, A., Huang, G.M., Wu, W.W. and Tseng, T.Y., 2018. Facile synthesis of mesoporous NiFe2O4/CNTs nanocomposite cathode material for high performance asymmetric pseudocapacitors. Applied Surface Science, 433, pp.1100-1112.

33. Xie, Y., Zhang, C., Hu, X., Zhang, C., Kelley, S.P., Atwood, J.L. and Lin, J., 2019. Machine learning assisted synthesis of metal–organic nanocapsules. Journal of the American Chemical Society, 142(3), pp.1475-1481.

34. Ward, L., Agrawal, A., Choudhary, A. and Wolverton, C., 2016. A general-purpose machine learning framework for predicting properties of inorganic materials. npj Computational Materials, 2(1), pp.1-7.

35. Graser, J., Kauwe, S.K. and Sparks, T.D., 2018. Machine learning and energy minimization approaches for crystal structure predictions: a review and new horizons. Chemistry of Materials, 30(11), pp.3601-3612.

36. Hautier, G., 2014. Data mining approaches to high-throughput crystal structure and compound prediction. Prediction and Calculation of Crystal Structures: Methods and Applications, pp.139-179.

37. Podryabinkin, E.V., Tikhonov, E.V., Shapeev, A.V. and Oganov, A.R., 2019. Accelerating crystal structure prediction by machine-learning interatomic potentials with active learning. Physical Review B, 99(6), p.064114.

38. Tawfik, S.A., Isayev, O., Stampfl, C., Shapter, J., Winkler, D.A. and Ford, M.J., 2019. Efficient prediction of structural and electronic properties of hybrid 2D materials using complementary DFT and machine learning approaches. Advanced Theory and Simulations, 2(1), p.1800128.

39. Wu, B., Han, S., Shin, K.G. and Lu, W., 2018. Application of artificial neural networks in design of lithium-ion batteries. Journal of Power Sources, 395, pp.128-136.

40. Sawant, V., Deshmukh, R. and Awati, C., 2023. Machine learning techniques for prediction of capacitance and remaining useful life of supercapacitors: A comprehensive review. Journal of Energy Chemistry, 77, pp.438-451.